An Inductive Power Transfer System With a High-Q Resonant Tank for Mobile Device Charging

Qifan Li and Yung C. Liang, *Senior Member, IEEE*

***Abstract*—Inductive power transfer (IPT), which employs the principle of electromagnetic induction, is widely applied to wireless charging applications. The efficiency of an IPT system is highly dependent on the quality factor (Q) of the power resonant tank. In this paper, a novel design on the structure of the resonant coil is used in the resonant tank to achieve a significantly high Q above 1000 for the IPT system. Compensating capacitors are used in both primary and secondary circuits to align the resonant frequencies in order for the system resonant status to be maintained by a frequency tracking circuit. The experimental results show that with a primary coil Q of 1200, the proposed IPT system allows power to be transferred at a maximum air gap distance to coil diameter ratio of 1.46 for a highest efficiency of 87% at the resonant frequency of 106 kHz.**

***Index Terms*—Inductive power transfer (IPT), quality factor (Q), resonant frequency tracking, wireless charging.**

I. Introduction

In recent years, mobile devices, such as cell phones and tablet computers, have become extremely popular for personal communication and business uses. Batteries of these mobile devices need regular recharging due to their limitation of battery capacity. The wireless power transfer (WPT) systems, which are designed to deliver power efficiently from a stationary primary source to one or more mobile secondary loads over an air gap, gain increasing attentions as a convenient approach for charging. The approach has the advantages of minimum or no external charging accessories, availability for multiple devices simultaneously, and a lower risk of electric shock. The WPT charging is also preferred for the implanted medical devices to power them through the skin rather than having wires penetrate the skin, which would increase the risk of infection.

The WPT charging may be achieved by different methods including microwave radiation [1], capacitive power transfer [2]–[4], and inductive power transfer (IPT) [5]–[8]. For the inductive coupling systems, they are used for both high- and low-power applications, such as to supply high power to monorail systems [9] and electric vehicles [10]–[12], or lower power to laptop computers [13] and mobile phones [14]–[17]. In 2009, the first standard on WPT developed by the Wireless Power Consortium, named Qi, was published for low power transfer up to 5 W and it marked the beginning of feasible use of contactless charging technology in portable commercial products [18].

Generally, an IPT system is implemented with specially constructed transformers, in which energy from the primary winding is transferred inductively through the air gap to the secondary winding. The power transmission efficiency greatly depends on the capability of energy delivered from the primary coil to the secondary coil. One factor which influences the amount of energy transferred is the coupling coefficient between the two coils. Due to the separation by the air gap, the coupling coefficient between the primary winding and the secondary winding is much smaller than that of conventional transformers, i.e., a smaller portion of the magnetic flux generated by the primary winding is received by the secondary winding. If the primary coil and the secondary coil are far apart or aligned with an angle, the amount of the magnetic flux generated by the primary coil which cuts through the secondary coil will be dramatically reduced, resulting in a smaller coupling coefficient and less power transferred. Another factor which affects the amount of energy transferred is the quality factor (Q) of the primary resonant coil at the resonant frequency. The value of Q reflects the ratio of the energy stored to the energy losses in the resonator per cycle. A higher value of Q indicates a greater resonant amplitude and a lower rate of energy loss relative to the stored energy in the resonator. When operated at the resonant frequency, the primary coil with higher Q generates a stronger ac magnetic field, which can be received easier or farther by the secondary coil. Therefore, the resonant frequencies of the primary and secondary coils are usually tuned to be the same by compensating capacitors in order to better transfer power to the secondary side over a longer distance with higher transfer efficiency.

In this paper, a new design on the resonant coil structure is implemented in the proposed IPT system to achieve a significantly high Q. Compared with conventional resonant coils made of litz wire, which usually have a Q with the value of several hundreds, the novel resonant coil is formed by integrating a stack of conductor and dielectric layers. This special topology allows a measured Q above 1000. Moreover, litz wire is more costly, especially for strand diameters below 50 μm less than the skin depth at a few megahertz. The proposed copper film with a thickness of 50 μm is less costly and widely available.

A block diagram of the proposed IPT system is shown in Fig. 1. In the circuit topology, the system consists of a primary-circuit subsystem and a secondary-circuit subsystem. At the primary side, a dc voltage is converted to a high-frequency pulsed voltage by the half-bridge inverter. The high-frequency pulsed

Manuscript received December 9, 2014; revised March 3, 2015; accepted April 8, 2015. Date of publication May 4, 2015; date of current version July 10, 2015. This work was supported by the Singapore National Research Foundation under its International Research Centre, Keio-NUS CUTE Centre at Singapore Funding Initiative and administered by the IDM Program Office. Recommended for publication by Associate Editor S.-C. Tan.

Q. Li is with the Department of Electrical and Computer Engineering, National University of Singapore, 119260 Singapore (e-mail: liqifan@nus.edu.sg).

Y. C. Liang is with the Department of Electrical and Computer Engineering, National University of Singapore, 119260 Singapore, He is also with the National University of Singapore Suzhou Research Institute, Suzhou 215123, China (e-mail: chii@nus.edu.sg).

Color versions of one or more of the figures in this paper are available online at http://ieeexplore.ieee.org.

Digital Object Identifier 10.1109/TPEL.2015.2424678

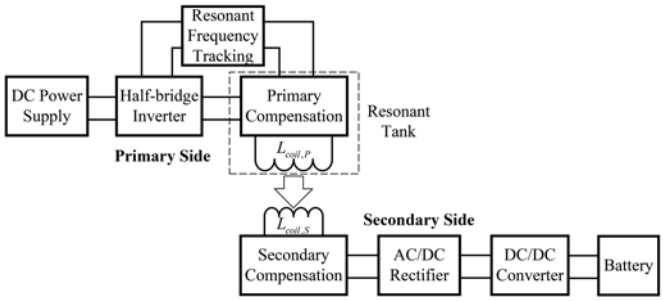

Fig. 1. Block diagram of the IPT system consisting of a primary-circuit subsystem and a secondary-circuit subsystem with inductive coupling in between.

voltage is then applied across the resonant tank, which contains a primary high-Q coil and a compensation capacitor. The frequency of the pulsed voltage is controlled by the phase-lock loop (PLL) feedback circuit so as to ensure that the resonant status of the resonant tank is always maintained. At the secondary side, a secondary coil is also connected to a compensating capacitor to align the resonant frequency. The ac voltage induced is rectified to become dc voltage and regulated by a dc–dc converter so as to generate a suitable dc voltage for mobile device charging.

In this paper, the topology of a high-Q resonant coil is described and analyzed in Section II. The resonant frequency of the coil is formulated by analyzing its circuit model and verified by prototypes fabricated. Section III describes the circuit design of the proposed IPT system. Finally, experimental results are shown in Section IV in order to verify the validity of the contactless power transfer system and evaluate the system performances.

II. High-Q Resonant Coil

A. Topology of the Resonant Coil

The high-Q resonant coil illustrated in Fig. 2 is formed by integrating stacked layers of conductor and dielectric and an open pot ferrite core [19]. Usually, a high-Q resonant coil consists of several repeating substacks, named sections, of the same stacking topology. In one section, starting with conductor layer at the bottom, dielectric layers and conductor layers are alternately stacked above, ending up with conductor layer on the lop, i.e., each two adjacent conductor layers in the section are separated by a dielectric layer in between. The top conductor layer has two terminals which are for the external connection. Aside from the top conductor layer, there are no other electrical contacts, no vias or external connections, in the rest of the structure of a section. Each dielectric layer is toroid shaped and each conductor layer is C shaped. The two successive C-shaped conductor layers face in opposite orientations and form two overlapping areas with a symmetric overlap angle θ defined as in Fig. 2. The overlapping areas of the conductor layers together with the dielectric layer between them form two capacitors within the sandwich unit. Current flowing in the inductive loop formed by the conductor layers passes through these two capacitors, denoted as C_0 in the equivalent circuit model.

The symmetric overlapping areas between two adjunct conductor layers are defined with an overlap angle θ. A unit is a substructure of two adjunct conductor layers and the ring-shaped dielectric layer between them.

B. Circuit Model and Analysis

Fig. 3 shows current distribution in the conductor layers by simulating a unit stack (two copper layers and one insulator layer) with an overlap angle θ at 170° on LTSPICE. The horizontal axis corresponds to the angular position φ from 0°, which refers to the central position of the open slot of the upper C-shaped conductor layer in the unit, in clockwise to 360°. The current through each conductor layer is normalized by its maximum value I_m, which happens at the nonoverlapping area opposite to the open slot of the C shape. In the conductor layer, the current flowing through varies with the angular position due to the current transfer between two conducting copper layers. In the overlapping region, the current transfers from one conductor layer to the adjacent ones and as a result, the current in a given conductor layer linearly increases or decreases as a function of the angular position. Hence, the current through the upper conductor layer in a unit $I_{c,\,\mathrm{upper}}$ can be represented as a function of the angular position φ as follows:

$$I_{c,\mathrm{upper}} = \begin{cases} \frac{I_m}{\theta}\left(\varphi - \frac{\pi-\theta}{2}\right), & \left(\frac{\pi-\theta}{2} \le \varphi < \frac{\pi+\theta}{2}\right) \\ I_m, & \left(\frac{\pi+\theta}{2} \le \varphi \le \frac{3\pi-\theta}{2}\right) \\ -\frac{I_m}{\theta}\left(\varphi - \frac{3\pi+\theta}{2}\right), & \left(\frac{3\pi-\theta}{2} < \varphi \le \frac{3\pi+\theta}{2}\right) \end{cases}. \tag{1}$$

Similarly, the current through the lower conductor layer in the unit $I_{c,\,\mathrm{lower}}$ is

$$I_{c,\,\mathrm{lower}} = \begin{cases} I_m, & \left(0 \le \varphi \le \frac{\pi-\theta}{2}\right) \\ -\frac{I_m}{\theta}\left(\varphi - \frac{\pi+\theta}{2}\right), & \left(\frac{\pi-\theta}{2} < \varphi \le \frac{\pi+\theta}{2}\right) \\ \frac{I_m}{\theta}\left(\varphi - \frac{3\pi-\theta}{2}\right), & \left(\frac{3\pi-\theta}{2} \le \varphi < \frac{3\pi+\theta}{2}\right) \\ I_m, & \left(\frac{3\pi+\theta}{2} \le \varphi < 2\pi\right) \end{cases}. \tag{2}$$

By adding $I_{c,\,\mathrm{upper}}$ and $I_{c,\,\mathrm{lower}}$, the loop current I_0 in the unit can be expressed as

$$I_0 = I_{c,\mathrm{upper}} + I_{c,\,\mathrm{lower}} = I_m, \quad (0 \le \varphi < 2\pi). \tag{3}$$

Therefore, the loop current I_0 in the unit is constant at all angular position φ and a lumped *RLC* equivalent circuit can be used to model the unit, as shown in Fig. 2. In the equivalent circuit, R_0 refers to the resistance of the conductor loop; L_0 refers to the inductance of the conductor loop; and C_0 refers to the capacitance of the capacitor formed by the overlapping area. For the analytical process of the single-layer planar *LC* structure, similar works were carried out in [20] and [21].

When the thickness of the conductor layer is less than the skin depth of the system operating frequency, the resistance of a single-layer loop can be approximated by its dc

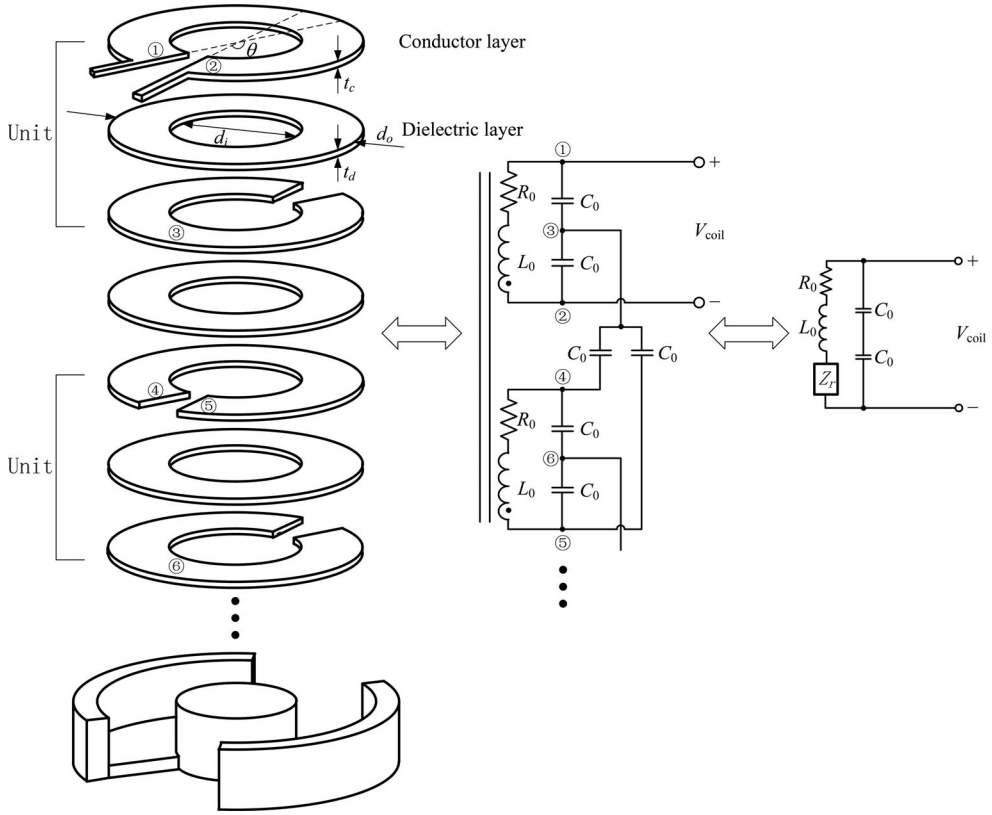

Fig. 2. Structure of the high-Q resonant coil which contains a stack of C-shaped conductor layers and ring-shaped dielectric layers, and its equivalent *RLC* resonant circuits.

resistance as

$$R_{\text{loop}} = \frac{1}{\int_{\frac{d_i}{2}}^{\frac{d_o}{2}} \frac{t_c\,dr}{2\pi\rho r}} = \frac{2\pi\rho}{t_c \ln\frac{d_o}{d_i}} \tag{4}$$

where ρ is the resistivity of the conductor used, t_c is the thickness of the conductor layer, and d_o and d_i are the outer and inner diameter of the conductor layer, respectively. Since current linearly increases or decreases over the distance of the overlap angle θ, the equivalent resistance of the conductor at overlapping area is halved in terms of the maximum current I_m. Thus, the equivalent resistance of a unit is derived as

$$R_0 = \frac{\theta R_{\text{loop}}}{2\pi} + \frac{(\pi-\theta)\,R_{\text{loop}}}{2\pi} = \frac{R_{\text{loop}}}{2} = \frac{\pi\rho}{t_c \ln\frac{d_o}{d_i}}. \tag{5}$$

Then, the expression of L_0, which is an approximate parallel-plate configuration [22], is derived as

$$L_0 = \frac{\mu_0\mu_r\,(d_o+d_i)}{4}\left[\ln\frac{8\,(d_o+d_i)}{d_o-d_i} - 2\right] \tag{6}$$

where μ_0 and μ_r are the vacuum and relative permeability.

Finally, the expression of C_0, which is also an approximate parallel-plate configuration, is derived as

$$C_0 = \frac{\varepsilon_0\varepsilon_r\theta\left(d_o^2-d_i^2\right)}{8t_d} \tag{7}$$

where ε_0 and ε_r are vacuum and relative permittivity, respectively, and t_d is the thickness of the dielectric layer.

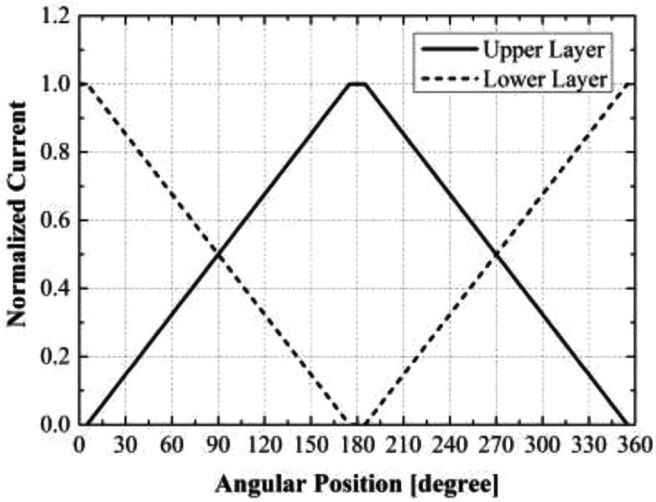

Fig. 3. Normalized current flowing through top and bottom layers of a unit versus angular position, starting from 0° referring to the central position of the open slot of the upper C shape, clockwise to 360°.

In the equivalent circuit of one section stack shown in Fig. 2, points ①–⑥ in the model are, respectively, corresponding to the physical points ①–⑥of the resonant coil. The value of the capacitors connecting two adjunct units is equal to C_0. Only the top unit has the connection to the external circuit. Currents in other units are induced by inductive coupling, which effectively

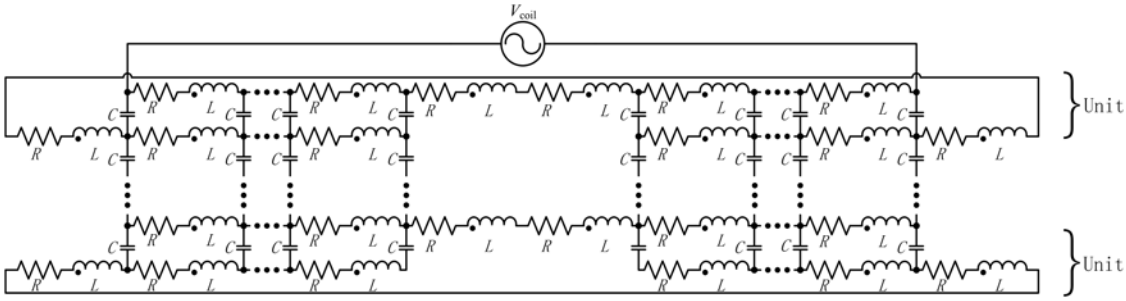

Fig. 4. Schematic diagram of the distributed element model for the proposed resonant coil used in LTSPICE simulation.

puts all the units in parallel. However, as the number of parallel units increases, the inductive coupling to the farther units becomes weaker and results in lower current through these units. Therefore, a high-Q resonant coil are usually divided into several sections, each containing several units in order to achieve strong coupling and effective current sharing in every conductor layer.

Assuming strong coupling between arbitrary two units due to the high permeability of ferrite core, i.e., the coupling coefficient is close to 1, the mutual inductance between each two units can be written as $M = L_0$. To calculate the resonant frequency of the whole stack, the impedance of the rest of the units is reflected to the first top unit, named Z_r as shown in Fig. 2. Due to the strong coupling, the model for each unit is the same except the top unit which has a connection to the external circuit. As for the unit without galvanic connections, there exists

$$Z_{0,(2)} = R_0 + j\omega L_0 + \frac{1}{j\omega C_0} \tag{8}$$

$$0 = j\omega M\left[I_{0,(1)} + (N-2)\, I_{0,(2)}\right] + Z_{0,(2)} I_{0,(2)} \tag{9}$$

where $Z_{0,(2)}$ is the impedance of the unit without galvanic connections to the external circuit, $I_{0,(1)}$ and $I_{0,(2)}$ are the loop currents through the top unit and the rest units, respectively, and N is the number of total units. We can derive $I_{0,(2)}$ in terms of $I_{0,(1)}$ as

$$I_{0,(2)} = -\frac{j\omega M}{R_0 + j\left[\omega L_0 + \omega M\,(N-2) - \frac{1}{\omega C_0}\right]} I_{0,(1)}. \tag{10}$$

Then, the expression of the reflected impedance of one unit Z_{r0} is

$$Z_{r0} = \frac{j\omega M I_{0,(2)}}{I_{0,(1)}} = \frac{\omega^2 M^2}{R_0 + j\left[\omega L_0 + \omega M\,(N-2) - \frac{1}{\omega C_0}\right]}. \tag{11}$$

The reflected resistance and reactance can be respectively derived as

$$\mathrm{Re}\,(Z_{r0}) = \frac{\omega^4 C_0^2 M^2 R_0}{\left\{\omega^2 C_0\left[L_0 + M\,(N-2)\right] - 1\right\}^2 + \omega^2 C_0^2 R_0^2} \tag{12}$$

$$\mathrm{Im}\,(Z_{r0}) = -\frac{\omega^3 C_0 M^2\left\{\omega^2 C_0\left[L_0 + M\,(N-2)\right] - 1\right\}}{\left\{\omega^2 C_0\left[L_0 + M\,(N-2)\right] - 1\right\}^2 + \omega^2 C_0^2 R_0^2}. \tag{13}$$

Typically, R_0, L_0, and C_0 are of the order of milliohm, microhenry, and nanofarad, respectively. Thus, (12) and (13) are approximately as

$$\mathrm{Re}\,(Z_{r0}) \approx \omega^4 C_0^2 M^2 R_0 \tag{14}$$

$$\mathrm{Im}\,(Z_{r0}) \approx \omega^3 C_0 M^2. \tag{15}$$

Due to the same topology of the units, the total reflected impedance Z_r is

$$Z_r = (N-1)\, Z_{r0}. \tag{16}$$

$$\mathrm{Re}\,(Z_{\mathrm{coil}}) = \frac{4\left[R_0 + (N-1)\,\omega^4 C_0^2 M^2 R_0\right]}{\left\{2 - \omega^2 C_0\left[L_0 + (N-1)\,\omega^2 C_0 M^2\right]\right\}^2 + \omega^2 C_0^2\left[R_0 + (N-1)\,\omega^4 C_0^2 M^2 R_0\right]^2} \approx \frac{4R_0}{\left\{2 - \omega^2 C_0\left[L_0 + (N-1)\,\omega^2 C_0 M^2\right]\right\}^2 + \omega^2 C_0^2\left[R_0 + (N-1)\,\omega^4 C_0^2 M^2 R_0\right]^2} \tag{17}$$

$$\mathrm{Im}\,(Z_{\mathrm{coil}}) = \frac{4\omega\left[L_0 + (N-1)\,\omega^2 C_0 M^2\right] - 2\omega C_0\left\{\left[\omega L_0 + (N-1)\,\omega^3 C_0 M^2\right]^2 + \left[R_0 + (N-1)\,\omega^4 C_0^2 M^2 R_0\right]^2\right\}}{\left\{2 - \omega^2 C_0\left[L_0 + (N-1)\,\omega^2 C_0 M^2\right]\right\}^2 + \omega^2 C_0^2\left[R_0 + (N-1)\,\omega^4 C_0^2 M^2 R_0\right]^2} \approx \frac{4\omega\left[L_0 + (N-1)\,\omega^2 C_0 M^2\right] - 2\omega^3 C_0\left[L_0 + (N-1)\,\omega^2 C_0 M^2\right]^2}{\left\{2 - \omega^2 C_0\left[L_0 + (N-1)\,\omega^2 C_0 M^2\right]\right\}^2 + \omega^2 C_0^2\left[R_0 + (N-1)\,\omega^4 C_0^2 M^2 R_0\right]^2} \tag{18}$$

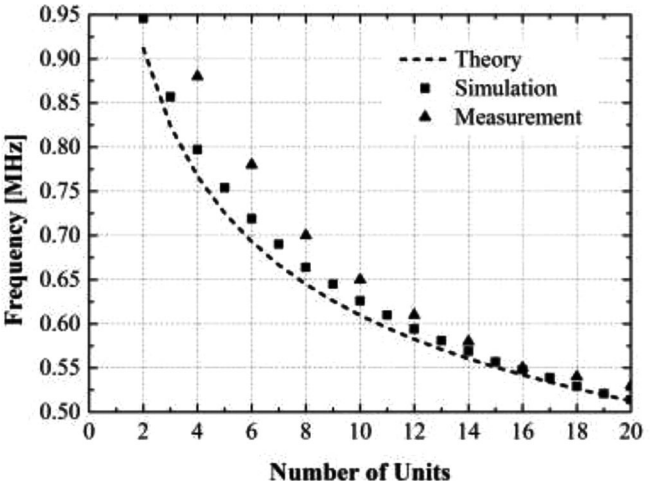

Fig. 5. Resonant frequency versus the number of coil units by theoretical calculations, simulations and experimental measurements.

TABLE I
DESIGN PARAMETERS OF THE HIGH-Q RESONANT COIL

Parameter	Value	Parameter	Value
Coil outer diameter	59 mm	Number of Units	16
Coil inner diameter	29 mm	Number of Sections	8
Thickness of conductor layer	50 μm	Relative permeability of ferrite core	2300
Thickness of dielectric layer	50 μm	Relative permittivity of dielectric	2.5
Overlap angle	170°	Relative permittivity of glue	2.0

Fig. 6. Photograph of the prototyped high-Q resonant coil with a measured Q of 1200 at the resonant frequency of 550 kHz.

In Fig. 5(b), the resistance and reactance of the total impedance $Z_{\rm coil}$ seen from the input voltage is derived as (17 and 18) as shown at the bottom of the previous page.

By setting the reactance of the total impedance equal to zero, the resonant frequency can be derived by solving the following equation:

$$0 = 4\left[L_0 + (N-1)\,\omega^2 C_0 M^2\right] - 2\omega^2 C_0\left[L_0 + (N-1)\,\omega^2 C_0 M^2\right]^2. \quad (19)$$

Typically, the number of units N is from tens to hundreds. Thus, the approximate solution of resonant frequency f_0 is

$$f_0 \approx \frac{\sqrt[4]{2}}{2\pi\sqrt{L_0 C_0}\sqrt[4]{N}}. \quad (20)$$

C. Simulation with Distributed Model

The resonant frequency of the resonant coil is determined by the equivalent inductance, the equivalent capacitance, and the number of units. The equivalent inductance and capacitance depend on the coil dimension, the overlap angle θ, the thickness of layers, the ferrite core material, etc. For example, the inductance will increase if ferrite material with higher permeability is utilized and the capacitance will increase if it has a larger overlapping area or the thickness of dielectric layers is reduced. In order to have a lower resonant frequency for a lower switching loss, the equivalent inductance and capacitance should be as large as possible. Copper sheet with a thickness of 50 μm and an overlap angle of 170° is used for conductor layers. Even at the maximum system frequency near 1 MHz, this thickness is smaller than the skin depth of copper, which is at 65 μm. Thus, using the dc resistance as an approximation is reasonable. The 50 μm NOMEX Type 410 insulation paper with a relative permittivity of 2.5 is employed for dielectric layer. A PM-type ferrite core made from N87 material, which has an initial relative permeability of 2300, is readily available. The outer and inner diameter of its winding area is 59 and 29 mm, respectively. Substituting these parameters in the coil structure to (5)–(7), we can calculate the parameters of the equivalent circuit as $R_0 = 1.504\,\mathrm{m\Omega}$, $L_0 = 70.28\,\mu$H, and $C_0 = 0.4335$ nF. Besides, a more effective way to reduce the resonant frequency is to increase the number of units. Thus, a distributed element model for the proposed resonant coil is established on LTSPICE to examine the relationship between the resonant frequency and the number of units. The schematic diagram of the distributed element model is shown in Fig. 4. In the schematic diagram, each conductor layer is divided into 70 equal parts representing an angle of 5° each. In each part, distributed resistance, inductance, and capacitance are calculated as

$$R = \frac{R_0}{70} = 21.49\,\mu\Omega, \quad L = \frac{L_0}{70} = 1.004\,\mu\mathrm{H},$$
$$C = \frac{C_0}{35} = 0.01239\,\mathrm{nF}. \quad (21)$$

The simulation results are shown in Fig. 5 for the relationship between the resonant frequency and different number of units. The simulation results meet the theoretical curve quite well, especially when the number of units gets larger. Next, the experimental measurement of prototypes will provide further verification.

D. Coil Prototypes with Measurements

The resonant frequencies of the prototype coils are measured and also plotted in Fig. 5 to further verify the theory and simulation on the resonant frequency. The discrepancies between the experiment and simulation are caused by the assumption used in simulation that the coils are tightly surrounded by a uniform ferrite when calculating the loop inductance L_0. However, in experiment, the size of the ferrite core is not adjustable and the winding area of the ferrite core is not completely filled

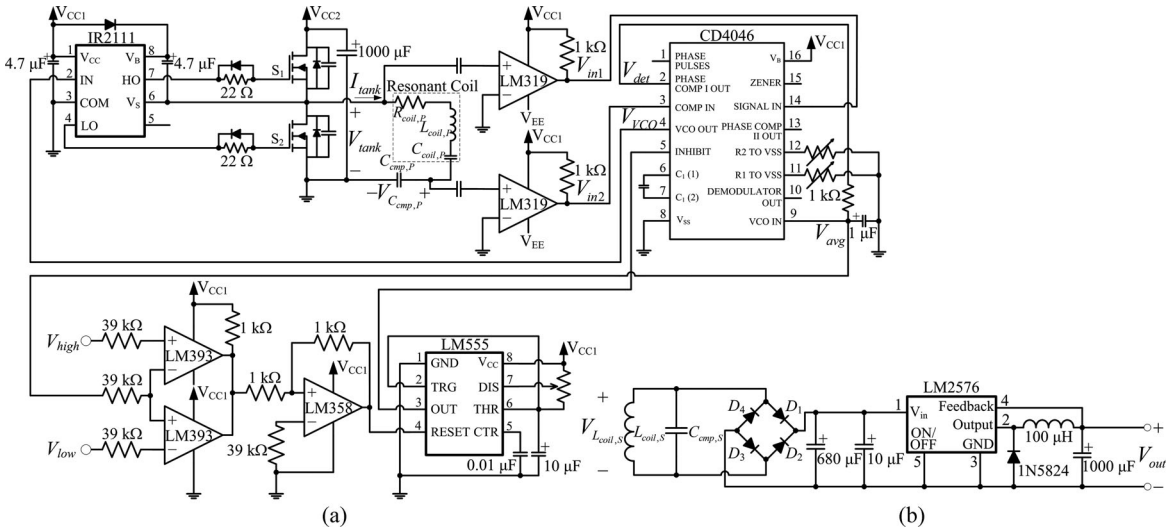

Fig. 7. Schematic of the IPT system: (a) Primary-circuit subsystem and (b) secondary-circuit subsystem.

up if the number of coil units is fewer, resulting in a decrease of self-inductance. However, an acceptable discrepancy of less than 4% is found when the number of coil units is at 14 or above. Considering the practical issues in coil construction, a 16-unit resonant coil is adopted in making the coil prototype in this paper. A summary of the parameters of the proposed high-Q resonant coil is listed in Table I. Water-based glue is used to stick two adjunct layers together. The stack is compressed by high pressure until extra glue exudes from the edges of the layers and until the glue solidifies. The average thickness of a glued layer is at about 3.3 μm, which is 6.6% of that of a dielectric layer. The relative permittivity of the glue used is measured to be 2.0, similar to that of dielectric layers of 2.5. Thus, the glue layer has little influence on the inter-layer capacitance according to the analysis in [23]. Finally, the stack is tightly compacted with multiple units and shown in Fig. 6, together with its measured Q of 1200 at the resonant frequency of 550 kHz.

In order to further lower the resonant frequency to be around 100 kHz, a compensating capacitor is added in series with the coil prototype to form a resonant tank, which will be described in Section III.

III. Proposed System Design

In this section, the design of the proposed IPT system is presented. There are two main features. One is to ensure that both the primary and secondary circuits are tuned to similar resonant frequencies for the optimal transfer range and efficiency. The other is to maintain the resonant status of the system by tracking the resonant frequency when the load at the secondary side varies.

A. Primary Circuit and Secondary Circuit

The IPT system is made of two main subsystems, namely primary circuit and secondary circuit as shown in Fig. 7. The operating frequency of the primary circuit is generated by the resonant frequency tracking unit which is to maintain the resonant status as the load on the secondary side changes. When the load on the secondary side is lacking or far from the primary coil, resulting in the resonant frequency beyond the preset range, a standby mode of the tracking unit will be started to save energy. This function is implemented in the primary circuit.

In the secondary circuit, the ac voltage across the secondary coil is rectified into dc voltage by the full-wave rectifier and converted to a constant and stable dc voltage at the dc–dc converter output. The output voltage of the dc–dc converter is easily adjustable for different charging applications.

B. Frequency Compensating Circuit

Depending on the serial (S) or parallel (P) connections of the compensating circuits in the primary and secondary circuit, there are four possible structures as SS, SP, PS, and PP [24]. The combination of serial and parallel connections is also used [25]. In the IPT system, we use serial structure in the primary circuit and parallel structure in the secondary circuit. The compensating capacitor at the secondary side is chosen by

$$f_{0,S} = \frac{1}{2\pi\sqrt{L_{\mathrm{coil},S}C_{cmp,S}}} \tag{22}$$

to be at 89 nF in order to achieve around the desired resonant frequency for the inductance of the secondary coil of 24 μH. Then, the compensating capacitor of at the primary side is chosen as 9.8 μF by the same process as that of the secondary side.

With the inclusion of the compensating capacitors, the resonant frequencies on both sides are tuned to be very close or the same. Considering the cost of the system, the resonant frequency around 100 kHz is employed due to the implementation by conventional silicon MOSFET and to lower the switching loss. The final measurement on the PCB prototype shows a resonant frequency of 106 kHz is achieved.

C. Resonant Frequency Tracking Unit

In order to maximize power transfer efficiency, the operating frequency of the IPT system should be closely tuned near

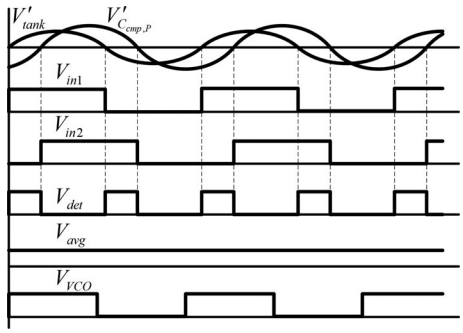

Fig. 8. Key waveforms of the resonant frequency tracking unit.

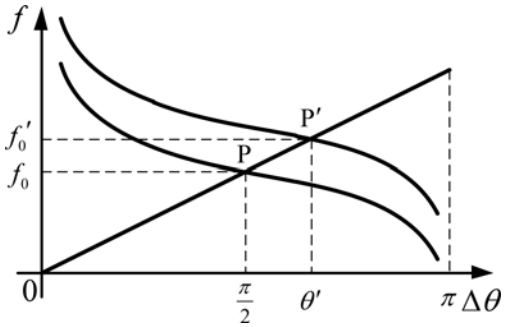

Fig. 9. State diagram of resonant frequency tracking.

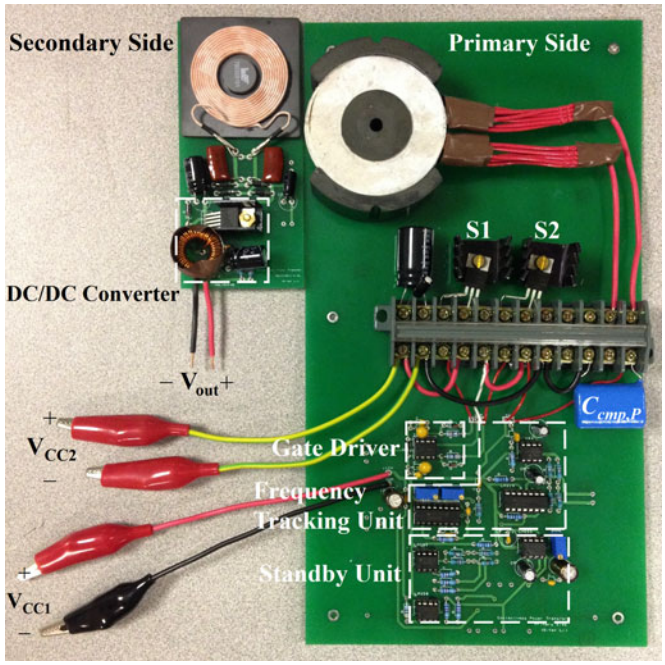

Fig. 10. Photograph of the prototyped IPT system.

the resonant frequency of the system. The resonant frequency tracking unit, which consists of a comparator circuit and a PLL circuit, can generate a square wave output with a frequency adjustment according to the phase difference between the two input signals. The two inputs are from the voltage across the resonant tank and the voltage across the compensating capacitor. First, the two sampled waveforms are converted into equal magnitude square waveforms by a zero-crossing detector circuit. Then, the two square waveforms $V_{\rm in1}$ and $V_{\rm in2}$ are sent to the phase detector of PLL chip, which generates a pulse voltage $V_{\rm det}$ representing the phase difference between the inputs. The generated voltage $V_{\rm det}$ passes through a low-pass filter and the average dc voltage $V_{\rm avg}$ proportional to the phase difference is then obtained. Finally, the voltage-controlled oscillator in the PLL chip generates a periodic square wave output $V_{\rm VCO}$ whose frequency is proportional to the dc voltage. This output is applied to the input of the half-bridge gate drive for the resonant tank. The waveforms described above are illustrated in Fig. 8.

When resonance occurs, the phase of the voltage across the resonant tank is 90° leading the phase of the voltage across the compensating capacitor. The center frequency of the PLL is set to be the resonant frequency when the secondary coil is best positioned next to the primary coil. When the secondary coil is moving away from the best position, the mutual inductance will decrease, which results in the increase of the system resonant frequency. The output of the frequency tracking unit will respond to compensate the change of the resonant frequency. The state diagram on the frequency tracking is illustrated in Fig. 9. The linear curve is the property of the resonant frequency tracking unit, representing the relationship between the phase difference at the two inputs and the tracking frequency at its output. The other curve is the property of the resonant tank, representing the relationship between the operating frequency and the phase difference between the two voltages across the tank and across the compensating capacitor. The operating point P is where the set center frequency equals to the system resonant frequency at the best coil positioning. A movement of the secondary coil leads to a raise of the property curve of the resonant tank. The new operating point is now the crossover point P′, which has a higher operating frequency than before to cater the change of the system resonant frequency. Starting at the center frequency at 106 kHz, a preset range of frequency tracking window from 40.6 to 172.3 kHz is configured by the external circuit of PLL chip. Within this frequency range, the resonant frequency tracking unit can keep the system operating frequency very close to the system resonant frequency. When the secondary coil is absent, the resonant frequency increases significantly, resulting that the operating point slips beyond the upper limit of the VCO frequency. Thus, the standby unit inhibits the PLL chip tracking for a short period for power saving. The hardware verification can be seen in Fig. 13 which is to be described later.

IV. Experimental Results and Discussion

Fig. 10 shows the prototyped IPT system, which includes a primary-circuit subsystem and a secondary-circuit subsystem. At the primary side, the control circuit is built on PCB and the high-Q resonant coil with its compensating capacitor is shown. At the secondary side, the coupling coil is a two-layer winding with a permanent magnetic core on a planar ferrite platform. The dimension of the secondary-circuit subsystem is 12.5 cm in

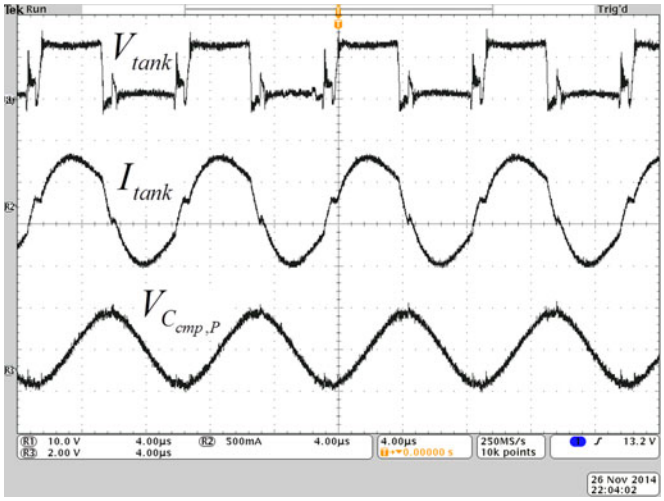

Fig. 11. Measured voltage waveforms across the resonant tank (upper trace, 10 V/div), compensating capacitor (lower trace, 2 V/div) and the current waveforms (middle trace, 500 mA/div) through the resonant tank at time scale of 4 μs/div.

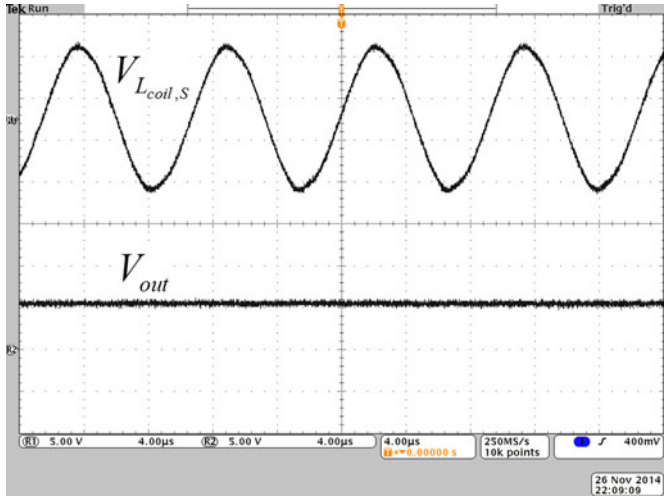

Fig. 12. Measured ac voltage across the secondary coil (upper trace, 5 V/div) and dc voltage across the rectifier output (lower trace, 5 V/div) at the time scale of 4 μs/div.

length and 6.3 cm in width, which is suitable for the fitting in most mobile phones.

In the test, the load is constant at 5 V, 1 A. Fig. 11 shows the waveforms of the voltage across the resonant tank and the voltage across the compensating capacitor. The current through the resonant tank is also shown. At the operating frequency of 106 kHz, the resonant tank has the voltage across the resonant tank and the current through the resonant tank is in the same phase, which indicates that the circuit operates in the resonant state. During the resonant state, the phase difference between the voltage across the resonant tank and the voltage across the compensating capacitor is at 90°, as tracked by the PLL circuit.

At the secondary side, the sinusoidal voltage across the secondary coil is induced. The voltage is rectified by a full-wave rectifier and converted to a constant and stable dc voltage as output. The induced sinusoidal voltage and the dc voltage are shown in Fig. 12.

As shown in Fig. 13, when the distance between the primary coil and the secondary coil increases, the resonant frequency of the system changes to be higher. The resonant frequency tracking unit tries to tune the operating frequency following the change of the resonant frequency. The tracking of the resonant frequency tracking unit is shown in Fig. 13, for example with the 7.6% maximum difference at the separation distance of 9 cm.

The load power at various coil distances is plotted in Fig. 14. The 5-W load power is maintained until the current in the primary circuit reaches its maximum limitation determined by the permissible rms current of 3.0 A in the primary compensating capacitor at 100 kHz and 85 °C. At the distance around 6 cm, the output power is reduced. The efficiency of the IPT system is calculated as the ratio between the energy transferred to load and the total energy at input. Fig. 15 shows that the highest efficiency measured is 87% where the two coils are placed closely without gap. The workable distance is up to 8.6 cm between

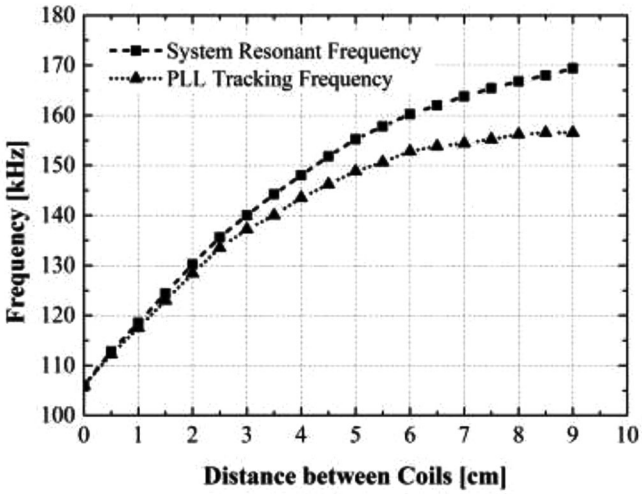

Fig. 13. Resonant frequency variations and PLL tracking versus the coil distance, indicating that the frequency tracking unit is capable of maintaining the circuit operation close to the resonant status.

the primary coil and the secondary coil with a power transfer efficiency of 10%.

The proposed IPT system with high-Q resonant coil is compared with the previous IPT system with traditional low-Q coil as reported in [18]. Both IPT systems use the same control circuit for frequency tracking and similar main circuit. The primary coil implemented in [18] is made of litz wire wound in a two-layer spiral shape on a ferrite plate with a cylindrical magnet in the center. Performances of the IPT systems are compared in Table II.

Fig. 16 makes performance comparison between the proposed system and published works on IPT system on the overall maximum power efficiency and the transmission distance ratio, which is the ratio of the maximum transmission distance $d_{\max}$ to the coil equivalent dimension D. The proposed IPT with a

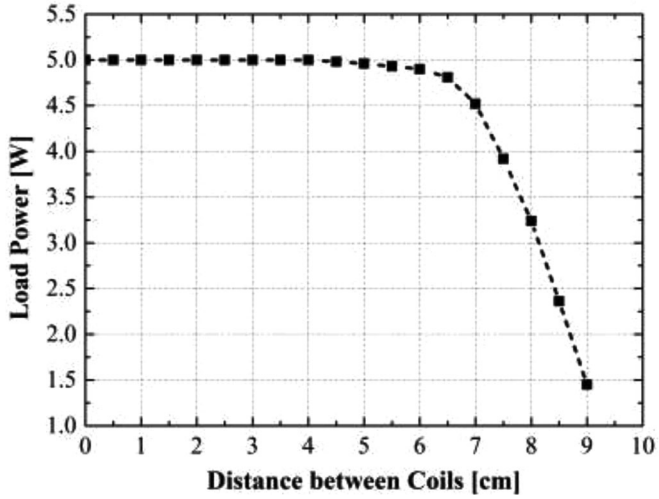

Fig. 14. Load power versus the coil distance.

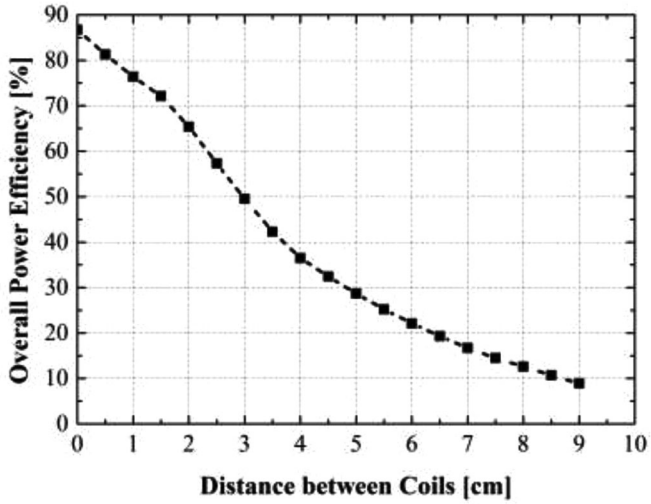

Fig. 15. Efficiency of power transferred versus the coil distance.

TABLE II
COMPARISONS BETWEEN IPT SYSTEMS WITH HIGH-Q COIL AND LOW-Q COIL

Parameter	IPT system with high-Q coil	IPT system with low-Q coil [18]
Q of the resonant tank with $C_{\mathrm{cmp,P}}$	240 (at 106 kHz) 160 (at 170 kHz)	90
Operating frequency	106 kHz	100 kHz
Power transfer efficiency	87%	45%
Maximum transmission distance	8.6 cm	3 cm
Transmission distance ratio	1.46	0.70
Maximum output power	5 W	0.75 W

maximum efficiency of 87% and the transmission distance ratio of 1.46 shows a relatively high performance compared to other works cited. This also verifies that the proposed IPT system is effective enough for the power transfer to mobile devices.

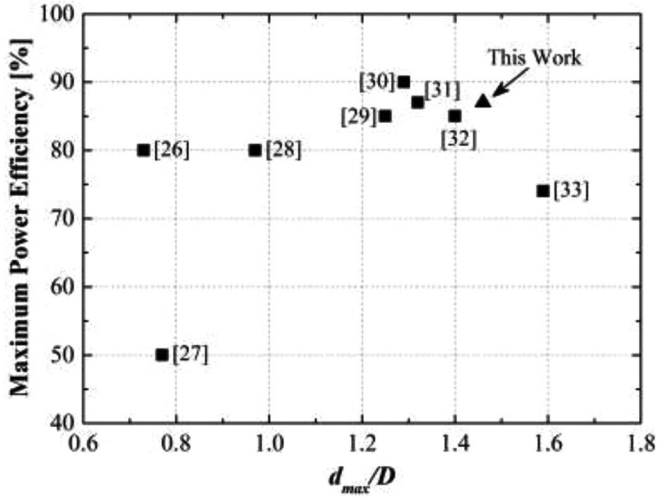

Fig. 16. Comparison of the maximum power efficiency and transmission capability with related works from [26]–[33].

V. CONCLUSION

In this paper, a contactless power transfer system with a high-Q resonant tank for mobile device charging application has been designed and implemented. To achieve significantly high Q, a specially structured resonant coil containing stacks of copper conductor and dielectric layers is properly made. The prototype of the resonant coil has measured with a Q value of 1200 at its self-resonant frequency of 550 kHz.

The performance of the proposed IPT system is experimentally measured. The highest power delivery efficiency is at 87% and the maximum transmission distance ratio is at 1.46. The proposed system is benchmarked with other related works as cited in the references to demonstrate its performance in effective power transfer for the charging of mobile devices.

REFERENCES

[1] C. Bergsrud and J. Straub, "A space-to-space microwave wireless power transmission experiential mission using small satellites," *Acta Astron.*, vol. 103, pp. 193–203, Oct.–Nov. 2014.

[2] M. Kline, I. Izyumin, B. Boser, and S. Sanders, "Capacitive power transfer for contactless charging," in *Proc. IEEE 26th Annu. Appl. Power Electron. Conf.*, 2011, pp. 1398–1404.

[3] C. Liu, A. P. Hu, B. Wang, and N. K. C. Nair, "A capacitively coupled contactless matrix charging platform with soft switched transformer control," *IEEE Trans. Ind. Electron.*, vol. 60, no. 1, pp. 249–260, Jan. 2013.

[4] M. P. Theodoridis, "Effective capacitive power transfer," *IEEE Trans. Power Electron.*, vol. 27, no. 12, pp. 4906–4913, Dec. 2012.

[5] C. Y. Huang, J. T. Boys, G. A. Covic, and M. Budhia, "Practical considerations for designing IPT system for EV battery charging," in *Proc. IEEE Veh. Power Propul. Conf.*, Sep. 2009, pp. 402–407.

[6] Z. Pantic, K. Lee, and S. M. Lukic, "Multifrequency inductive power transfer," *IEEE Trans. Power Electron.*, vol. 29, no. 11, pp. 5995–6005, Nov. 2014.

[7] W. Zhang, S. C. Wong, C. K. Tse, and Q. H. Chen, "Analysis and comparison of secondary series- and parallel-compensated inductive power transfer systems operating for optimal efficiency and load-independent voltage-transfer ratio," *IEEE Trans. Power Electron.*, vol. 29, no. 6, pp. 2979–2990, Jun. 2014.

[8] H. Hao, G. A. Covic, and J. T. Boys, "A parallel topology for inductive power transfer power supplies," *IEEE Trans. Power Electron.*, vol. 29, no. 3, pp. 1140–1151, Mar. 2014.
[9] G. A. J. Elliott, G. A. Covic, D. Kacprzak, and J. T. Boys, "A new concept: Asymmetrical pick-ups for inductively coupled power transfer monorail systems," *IEEE Trans. Magn.*, vol. 42, no. 10, pp. 3389–3391, Oct. 2006.
[10] F. Musavi and W. Eberle, "Overview of wireless power transfer technologies for electric vehicle battery charging," *IET Power Electron.*, vol. 7, pp. 60–66, Jan. 2014.
[11] U. K. Madawala and D. J. Thrimawithana, "A bidirectional inductive power interface for electric vehicles in V2G systems," *IEEE Trans. Ind. Electron.*, vol. 58, no. 10, pp. 4789–4796, Oct. 2011.
[12] C. Duan, C. G. Jiang, A. Taylor, and K. Bai, "Design of a zero-voltage-switching large-air-gap wireless charger with low electric stress for electric vehicles," *IET Power Electron.*, vol. 6, pp. 1742–1750, Nov. 2013.
[13] Y. L. Ban, J. H. Chen, J. L. W. Li, and W. Hu, "Printed wideband notched antenna for wireless USB dongle attached to laptop computer," *J. Electromagn. Waves Appl.*, vol. 27, pp. 257–266, Jan. 2013.
[14] M. Fareq, M. Fitra, M. Irwanto, S. Hasan, and M. Arinal, "Low wireless power transfer using inductive coupling for mobile phone charger," presented at the Int. Conf. Sci. Eng. Math., Chem. Phys., Jakarta, Indonesia, 2014, vol. 495.
[15] V. Boscaino, F. Pellitteri, L. Rosa, and G. Capponi, "Wireless battery chargers for portable applications: Design and test of a high-efficiency power receiver," *IET Power Electron.*, vol. 6, pp. 20–29, 2013.
[16] L. Olvitz, D. Vinko, and T. Svedek, "Wireless power transfer for mobile phone charging device," in *Proc. IEEE 35th Int. MIPRO Conven.*, 2012, pp. 141–145.
[17] M. Fitra, M. Irwanto, H. S. Syafruddin, N. Gomesh, S. Farrah, and M. Rozailan, "Solar wireless power transfer using inductive coupling for mobile phone charger," in *Proc. IEEE 8th Int. Conf. Power Eng. Optim.*, 2014, pp. 473–476.
[18] X. Chen and Y. C. Liang, "Contactless power delivery for mobile device charging applications," in *Proc. IEEE 14th Workshop Control Model. Power Electron.*, 2013, pp. 1–4.
[19] C. R. Sullivan and L. Beghou, "Design methodology for a high-Q self-resonant coil for medical and wireless-power applications," in *Proc. IEEE 14th Workshop Control Model. Power Electron.*, 2013, pp. 1–8.
[20] O. H. Stielau, J. D. van Wyk, M. Ehsani, and I. J. Pitel, "Integrated reactive components in power electronic circuits," in *Proc. IEEE Power Electron. Spec. Conf.*, 1990, pp. 831–838.
[21] M. C. Smit, J. A. Ferreira, and J. D. van Wyk, "Technology for manufacture of integrated planar LC structures for power electronic applications," in *Proc. Eur. Conf. Power Electron. Appl.*, 1993, vol. 2, pp. 173–178.
[22] X. Liu and S. Y. Hui, "Optimal design of a hybrid winding structure for planar contactless battery charging platform," in *Proc. IEEE 41st Annu. Meeting Ind. Appl. Soc.*, 2006, pp. 2568–2575.
[23] B. Ge, D. C. Ludois, and R. Rerez, "The use of dielectric coatings in capacitive power transfer systems," in *Proc. IEEE Energy Convers. Congr. Expo.*, 2014, pp. 2193–2199.
[24] S. Hasanzadeh and S. Vaez-Zadeh, "Efficiency analysis of contactless electrical power transmission systems," *Energy Convers. Manage.*, vol. 65, pp. 487–496, Jan. 2013.
[25] Z. Pantic, S. Bai, and S. M. Lukic, "ZCS LCC-compensated resonant inverter for inductive-power-transfer application," *IEEE Trans. Ind. Electron.*, vol. 58, no. 8, pp. 3500–3510, Aug. 2011.
[26] I. F. Zambari, C. Y. Hui, and R. Mohamed, "Development of wireless energy transfer module for solar energy harvesting," in *Proc. 4th Int. Conf. Electr. Eng. Inf.*, 2013, pp. 882–894.
[27] Q. W. Yuan, Q. Chen, L. Li, and K. Sawaya, "Numerical analysis on transmission efficiency of evanescent resonant coupling wireless power transfer system," *IEEE Trans. Antennas Propag.*, vol. 58, no. 5, pp. 1751–1758, May 2010.
[28] A. O. Di Tommaso, F. Genduso, and R. Miceli, "A small power transmission prototype for electric vehicle wireless battery charge applications," in *Proc. Int. Conf. Renewable Energy Res. Appl.*, 2012, pp. 1–6.
[29] S. Hasanzadeh, S. Vaez-Zadeh, and A. H. Isfahani, "Optimization of a contactless power transfer system for electric vehicles," *IEEE Trans. Veh. Technol.*, vol. 61, no. 8, pp. 3566–3573, Oct. 2012.
[30] H. Takanashi, Y. Sato, Y. Kaneko, S. Abe, and T. Yasuda, "A large air gap 3 kW wireless power transfer system for electric vehicles," in *Proc. IEEE Energy Convers. Congr. Expo.*, 2012, pp. 269–274.
[31] W. S. Lee, W. I. Son, K. S. Oh, and J. W. Yu, "Contactless energy transfer systems using antiparallel resonant loops," *IEEE Trans. Ind. Electron.*, vol. 60, no. 1, pp. 350–359, Jan. 2013.
[32] T. C. Beh, M. Kato, T. Imura, S. Oh, and Y. Hori, "Automated impedance matching system for robust wireless power transfer via magnetic resonance coupling," *IEEE Trans. Ind. Electron.*, vol. 60, no. 9, pp. 3689–3698, Sep. 2013.
[33] J. Huh, S. W. Lee, W. Y. Lee, G. H. Cho, and C. T. Rim, "Narrow-width inductive power transfer system for online electrical vehicles," *IEEE Trans. Power Electron.*, vol. 26, no. 12, pp. 3666–3679, Dec. 2011.

Qifan Li received the B.S. degree in electrical engineering from Xi'an Jiaotong University, Xi'an, China, in 2013. He is currently working toward the M.Eng. degree with the Power Electronics Laboratory, National University of Singapore, Singapore.

His research interests include wireless power transfer and power electronics.

Yung C. Liang (S'85–M'86–SM'00) received the M.Sc. degree from National Tsing Hua University, Hsinchu, Taiwan, in 1985, and the Ph.D. degree from the University of Sydney, Sydney, Australia, in 1991, both in electrical engineering.

He is currently an Associate Professor with the Department of Electrical and Computer Engineering, National University of Singapore, Singapore. His research interests include power microelectronics, silicon microsystems, microfuel cells, and ferroelectric devices. He has more than 180 journal and conference publications in these areas.

Dr. Liang served as the Chairman of the IEEE Singapore Section during 1998–1999. He received the IEEE Third Millennium Medal and the IEEE PELS Transactions Paper Prize on high-frequency smart power synchronous rectifiers in 2000. He is the founding Adcom Member for the IEEE International Conference on Power Electronics and Drive Systems and the IEEE International Conference on Sustainable Energy Technologies. He currently serves as an Associate Editor for the IEEE TRANSACTIONS ON POWER ELECTRONICS and the *International Journal of Power Electronics*.